JOURNAL OF MATERIALS SCIENCE 32 (1997) 6269–6278

Mathematical model for laser densification of ceramic coating

J. CHENG, A. KAR
Center for Research and Education in Optics and Lasers (CREOL), Mechanical, Materials and Aerospace Engineering Department, University of Central Florida, Orlando, FL 32816-2700 USA

A theoretical study for the densification of ceramic coating processed with a moving transmission electron microscopy (TEM_{00}) mode laser beam is conducted. A three-dimensional quasi-steady state heat conduction model is developed by applying the Fourier integral transform method. An approximate expression for temperature distribution is also presented and the calculations with it are found to be in good agreement with the exact solutions within a limited region around the laser spot. The depth of the heat-affected zone in ZrO_2 coating is calculated with this model. Moreover, a working range for ZrO_2 densification is determined by varying the laser beam power, spot size and scanning velocity. The heat-affected zone is found to be confined within a depth of 50 μm from the surface and the vitrified layers are fully densified for particles of initial radius 5 μm.

Nomenclature

A	Absorptivity of the workpiece
I	Laser power intensity ($W\,m^{-2}$)
k	Thermal conductivity ($W\,m^{-1}\,K^{-1}$)
k_0, k_1	Coefficients for approximate expression
P	Total power supply of the heat source (W)
r_0	Laser beam spot radius (m)
r_s	Initial radius of the particle (10^{-6} m)
T_m	Melting temperature of workpiece (K)
t	Isothermal sintering time (s)
x, y, z	Cartesian coordinates (m)
r', ϕ	Cylindrical coordinates (m, rad)
U	Laser beam scanning velocity ($m\,s^{-1}$)
α	Thermal diffusivity ($m^2\,s^{-1}$)
ρ'	Relative density (bulk density divided by true density, or fraction of true density reached)
γ	Surface tension ($N\,m^{-1}$)
η	Viscosity ($N\,s\,m^{-2}$)

1. Introduction

The carbon dioxide laser, a concentrated energy source, has been widely used as a heat source for surface treatment of engineering materials. Laser sintering of ceramic coating is a novel application of the laser materials processing technology. As a heat source, the laser has several advantages: it can (1) serve as a concentrated heat source of very high heat flux, (2) generate high temperatures instantaneously, (3) provide localized heating, and (4) allow easy control of the sintering atmosphere. These advantages make lasers attractive for sintering ceramic coatings.

To determine the temperature profile during laser treatment, many models have been developed to successfully explain and predict the effects of laser-induced heating and melting of materials. One of the earliest works on the energy distribution in the substrate during laser heating is due to Cline and Anthony [1]. They developed a time-dependent solution using Green's function for a scanning Gaussian beam. Lax [2, 3] analysed the heat conduction process in a cylindrical medium due to a stationary Gaussian beam under steady-state conditions by considering both constant and temperature-dependent thermophysical properties for the substrate. In the case of temperature-dependent thermophysical properties, Lax solved the problem by linearizing it with a Kirchoff transformation [4]. Hess *et al.* [5] derived the quasi-steady-state temperature distribution in a radially infinite cylindrical medium with temperature-dependent thermal conductivity by neglecting the effect of the laser beam scanning velocity. Nissim *et al.* [6] analysed the effects of elliptical and circular spots on the temperature distribution in semiconductors. Moody and Handel [7] used a numerical algorithm to calculate the temperature distribution in an infinite medium during laser heating. Modest and Abakians [8] examined the heat conduction in a moving semi-infinite solid subjected to a pulsed, penetrating, Gaussian laser source. Maier and co-workers [9] calculated the temperature profile during laser material processing with different kinds of laser processes, such as single-pass laser, multipass laser and pulsed laser treatment, and with a rectangular or a gaussian laser beams. Sander [10] analysed the temperature rise as a function of the ratio of the laser scanning speed to the heat diffusion in the solid and the ratio of the beam radius to the absorption depth. Kar and Mazumder [11] presented a three-dimensional transient thermal model to determine the temperature distribution

0022–2461

in a uniformly moving finite slab by considering temperature-dependent thermophysical properties and laser irradiation with a Gaussian beam. Manca *et al.* [12] presented an analytical solution to the three-dimensional quasi-stationary problem in a solid of finite depth and width for a circular Gaussian laser beam.

Chia *et al.* [13] developed a three-dimensional laser densification model to simulate the temperature distribution in a silica glass irradiated by a moving CO_2 laser. Both the reflectivity and the glass surface and the strong attenuation of the laser energy in the glass medium are accounted for by a detailed radiation analysis. Okutomi and Tsukamoto [14] investigated the sintering and growth of ceramics in the systems of ZrO_2–HfO_2, PSZ–HfO_2 and Al_2O_3–WO_3 by using a CO_2 laser beam as a heat source. This method will be practically useful for the synthesis of oxide, nitride, carbide and boride materials which have high hardness and high melting points. Kasai *et al.* [15] carried out the investigation of laser-sintered $BaTiO_3$. They concluded that an anomalous sintering behaviour at the microscopic level may occur since rapid heating by laser irradiation instantaneously raises the temperature of the particle surfaces.

In this paper, the heat conduction equation is solved to determine the temperature distribution in the workpiece by a scanning laser beam, and then this temperature distribution is utilized to investigate the thickness of the ceramic coating that can be densified during laser treatment. The theoretical prediction is found to be in good agreement with the results of experimental study [21]. A simple expression for the temperature distribution that can be obtained from the exact analytical solution of the heat conduction problem is also presented in this paper.

2. Mathematical model

2.1. Thermal modelling

To develop a thermal model for the laser densification process, a rectangular geometry is used as shown in Fig. 1. A focused CO_2 laser beam moves at a constant speed U in the positive x direction. The mathematical model is based on the following assumptions:

1. The properties of the sintering material, such as thermal conductivity, thermal diffusivity and absorptivity are independent of temperature.

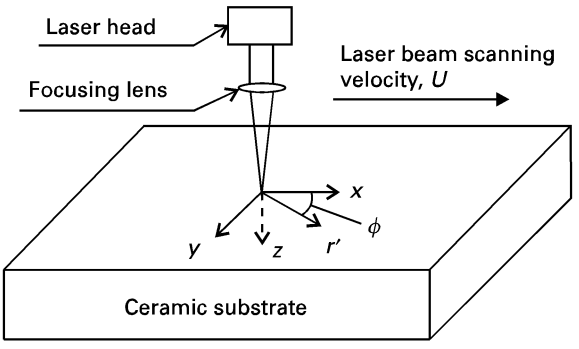

Figure 1 The geometry of laser beam relative to the substrate and the coordinate system.

2. Surface heat losses by convection and radiation are very small compared to heat conduction in the substrate i.e. they are neglected.

3. Lasers penetrate into the bulk of the material for many ceramics and deposits energy inside the material as it propagates through the medium. In this study, the laser energy is absorbed in an infinitely thin surface layer so that the laser energy absorption can be assumed to occur at the substrate surface.

The origin of the chosen coordinate system lies on the surface of the workpiece and coincides with the centre of the laser beam (see Fig. 1). The laser beam moves in positive x direction with a constant velocity U. Therefore, a quasi-steady state heat transfer condition is achieved after the laser beam travels a long distance. The heat conduction problem can be formulated mathematically as follows [16]

Governing equation

$$\frac{\partial^2 T^*}{\partial x^2} + \frac{\partial^2 T^*}{\partial y^2} + \frac{\partial^2 T^*}{\partial z^2} = -\frac{U}{\alpha}\frac{\partial T^*}{\partial x} \qquad x, y \to \pm\infty,\ 0 < z < \infty \tag{1}$$

Boundary conditions

$$T^*(x, y, z) = 0 \qquad \text{as } x, y \to \pm\infty,\ z \to \infty \tag{2}$$

$$\frac{\partial T^*}{\partial z} = -\frac{I^*}{k(T_m - T_i)} \qquad \text{at } z = 0 \tag{3}$$

The temperature $T^*(x, y, z)$, in Equation 1 is the dimensionless temperature of the workpiece, and is defined by

$$T^* = \frac{T_l - T_i}{T_m - T_i} \tag{4}$$

Here α and k are the thermal diffusivity and the reference thermal conductivity of the workpiece, respectively. In this study, k has a value $k = (k_x k_y k_z)^{1/3}$, where k_x, k_y and k_z are the principal values of thermal conductivity in x, y and z directions [17]. T_l, T_i are the actual and initial temperature of the substrate, respectively.

The intensity profile of the beam is Gaussian along both axes when the laser operates in the transmission electron microscopy (TEM_{00}) mode [18]

$$I^* = \frac{2AP}{\pi r_0^2}\exp\left[-\frac{2(x^2 + y^2)}{r_0^2}\right] \tag{5}$$

where P is the total power of the incident laser beam, A is the absorptivity of the workpiece, r_0 is the spot radius of the laser beam at $1/e^2$ point, and x and y are distances measured in Cartesian coordinates from the centre of the laser beam.

In order to simplify Equation 1, we define

$$T^* = T\exp(-bx) \qquad \text{where } b = \frac{U}{2\alpha} \tag{6}$$

Substituting Equation 6 into Equations 1–3 yields

$$\frac{\partial^2 T}{\partial x^2} + \frac{\partial^2 T}{\partial y^2} + \frac{\partial^2 T}{\partial z^2} = b^2 T \tag{7}$$

$$T(x, y, z) = 0 \qquad \text{as } x, y \to \pm\infty,\ z \to \infty, \tag{8}$$

$$\frac{\partial T}{\partial z} = -\frac{I^*\exp(bx)}{k(T_m - T_i)} = -I \qquad \text{at } z = 0 \tag{9}$$

The above problem defined by Equations 7–9 is solved by successively applying Fourier transforms in the x, y and z directions. The multiple Fourier transform in the x and y directions is

$$\bar{T}(\beta, \gamma, z) = \int_{-\infty}^{\infty} \int_{-\infty}^{\infty} \exp(i\beta x) \exp(i\gamma y) T(x, y, z) \, dx \, dy \quad (10)$$

The inversion formula is

$$T(x, y, z) = \frac{1}{4\pi^2} \int_{-\infty}^{\infty} \int_{-\infty}^{\infty} \exp(-i\beta x) \times \exp(-i\gamma y) \bar{T}(\beta, \gamma, z) \, d\beta \, d\gamma \quad (11)$$

Applying the integral transform Equation 10, to Equations 7–9, the following ordinary differential equation is obtained

$$\frac{\partial^2 \bar{T}}{\partial z^2} - (b^2 + \beta^2 + \lambda^2)\bar{T} = 0 \quad (12)$$

which must satisfy the following boundary conditions

$$\bar{T}(\beta, \gamma, z) = 0 \quad \text{as } z \to \infty \quad (13)$$

$$\frac{\partial \bar{T}}{\partial z} = -\bar{I} \quad \text{at } z = 0 \quad (14)$$

where

$$\bar{I} = \int_{-\infty}^{\infty} \int_{-\infty}^{\infty} \exp(i\beta x) \exp(i\gamma y) I \, dx \, dy$$

The solution to Equation 12 that satisfies the boundary condition Equations 13 and 14 can be written as

$$\bar{T}(\beta, \gamma, z) = \bar{I} \frac{\exp[-(b^2 + \beta^2 + \gamma^2 z)^{1/2}]}{(b^2 + \beta^2 + \gamma^2)^{1/2}} \quad (15)$$

Noticing that the Fourier inverse transform of $\exp[-(b^2 + \beta^2 + \gamma^2 z)^{1/2}]/(b^2 + \beta^2 + \gamma^2)^{1/2}$ is given by

$$\mathscr{F}^{-1} \left\{ \frac{\exp[-(b^2 + \beta^2 + \gamma^2 z)^{1/2}]}{(b^2 + \beta^2 + \gamma^2)^{1/2}} \right\} = \frac{1}{4\pi^2} \int_{-\infty}^{\infty} \int_{-\infty}^{\infty} \exp(-i\beta x) \exp(-i\gamma y) \times \frac{\exp[-(b^2 + \beta^2 + \gamma^2 z)^{1/2}]}{(b^2 + \beta^2 + \gamma^2)^{1/2}} \, d\beta d\gamma = \frac{1}{2\pi} \frac{\exp[-b(r^2 + z^2)^{1/2}]}{(r^2 + z^2)^{1/2}}$$

where $r = (x^2 + y^2)^{1/2}$ (16)

The convolution theorem is used to obtain an expression for $T(x, y, z)$ from Equation 15, and then the following expression for the dimensionless temperature $T^*(x, y, z)$ is determined from Equation 6

$$T^*(x, y, z) = 2 \int_0^{\pi} \int_0^{\infty} \frac{PA}{(\pi r_0)^2 k(T_m - T_0)} \exp\left[-br' \cos\phi - \frac{2(x - r' \cos\phi)^2 + 2(y - r' \sin\phi)^2}{r_0^2} \right] \times \frac{\exp[-b(r'^2 + z^2)^{1/2}]}{(r'^2 + z^2)^{1/2}} \, r' \, dr' \, d\phi \quad (17)$$

The actual temperature $T_1(x, y, z)$ can be obtained by substituting Equation 17 into Equation 4. $T^*(x, y, z)$ is calculated from Equation 17 by carrying out numerical integration.

Equation 17 can also be simplified (see Appendix) to obtain an approximate expression for the temperature distribution as given by Equation 18. There is a small region within which the results obtained from Equation 18 are very close (within 10%) to the results calculated by using Equation 17

$$T^*(x, y, z) = \frac{k_0 PA}{\pi r_0^2 k(T_m - T_i)} \exp\left(\frac{-2x^2 - 2y^2}{r_0^2} \right) \times \exp(-bz) \left[b + 0.5bk_1 - \frac{2(k_1 x + y)}{r_0^2} \right]^{-1} + \left[b - 0.5bk_1 + \frac{2(k_1 x - y)}{r_0^2} \right]^{-1}$$

$$-2.0 \text{ mm} \leqslant x < \infty \quad -r_0 < y < r_0 \quad 0 < z \leqslant 50 \, \mu\text{m} \quad (18)$$

where k_0 and k_1 are two coefficients that can vary with the laser beam scanning velocity, absorbed power and laser beam radius. The physical meanings of k_0 and k_1 are that k_0 scales the peak temperature and that k_1 scales the location of the peak temperature along the x-axis. These two parameters are discussed in Section 3.2 in which k_0 and k_1 are used for calculating temperature distribution along the x-axis ($y = 0$).

2.2. Densification modelling

The densification of a particulate ceramic compact is technically referred to as sintering. Sintering is essentially a heat treatment process that involves a removal of pores in the starting ceramic workpiece (accompanied by shrinkage of the component), combined with growth and strong bonding between adjacent particles.

Liquid-phase sintering is an important means of manufacturing dense ceramic components from powder compacts. Various technically important ceramics are manufactured by liquid-phase sintering. Liquid-phase sintering involves the presence of a viscous liquid at the sintering temperature. Three factors that control the rate of liquid phase sintering are (i) particle size, (ii) viscosity, and (iii) surface tension. It is well known that a small amount of liquid forming additives significantly enhances the densification kinetics in the liquid-phase sintering process. Less than 1 vol % liquid phase is sufficient to coat the grain

when the liquid is distributed uniformly in a material with a nominally 1 μm grain size [19].

Kingery *et al.* [20] presented the following expression for calculating the ceramics densification rate during the viscous liquid phase sintering

$$\frac{d\rho'}{dt} = \frac{3\gamma}{2r_s\eta}(1-\rho') \quad (19)$$

The densification rate is directly proportional to the surface tension, inversely proportional to the viscosity, and inversely proportional to the particle size of the ceramic compact.

The relative density is obtained by integrating Equation 19 and is given by

$$\rho' = 1-\exp\left(-\frac{3\gamma}{2r_s\eta}t\right) \quad (20)$$

As the laser beam travels in the positive x direction with a constant velocity, the points on the surface and those under the surface experience a Gaussian-like temperature field which decreases with increasing depth from the substrate surface.

It should be noted that vitrifying refers to making glasslike substances and that Equation 19 was obtained for the vitrification process, which refers to densification with the help of a viscous liquid phase. The rate of liquid-phase densification is strongly affected by the temperature. For most cases, a small increase in temperature results in the formation of a substantial amount of liquid. In some cases, this can be beneficial because it increases the rate of densification. In other cases, this can be detrimental because it causes excessive grain growth which reduces the strength of the material, and because it can slump and deform the workpiece [20]. Since the maximum temperature occurs at the substrate surface, the amount of the viscous ZrO_2 liquid present at the surface within the selected temperature range is larger than that below the surface. The solid particles are wetted by the viscous liquid. The liquid in the narrow channels between the particles results in substantial capillary pressure that aids densification.

However, liquid phase densification causes surface cracking [21]. For this reason, solid phase densification is considered in this paper where the sintering time is taken as the duration in which the temperature of any point remains between $0.75\,T_m$ and $0.95\,T_m$. The lower limit of temperature is chosen to be $0.75\,T_m$ because the diffusion of various species in the compact is the main mechanism for solid phase densification, and the diffusion is expected to be less significant below $0.75\,T_m$. The upper limit of the temperature range is chosen to be $0.95\,T_m$ because solid phase densification is investigated in this paper. Above this temperature, the compact will be close to its melting temperature and can exhibit highly viscous liquid-like phase. Under this condition, the vitrification of ZrO_2 particles is investigated in this paper using Equation 20, where the particles are considered to vitrify during the above-mentioned sintering time.

3. Results and discussion

The foregoing thermal and densification models are used in this section to analyse the temperature distribution and the relative density in the ZrO_2 ceramic substrate. The values of the material properties and the laser parameters used for this study are listed in Table I.

3.1. Temperature distributions using the exact solution

Equation 17 is used to calculate the temperature distribution $T^*(x, y, z)$, in ZrO_2 substrate by using the data listed in Table I. Fig. 2 represents a three-dimensional view of the temperature distribution on the top surface of the substrate. It can be seen that the shape of the surface temperature field has Gaussian-like

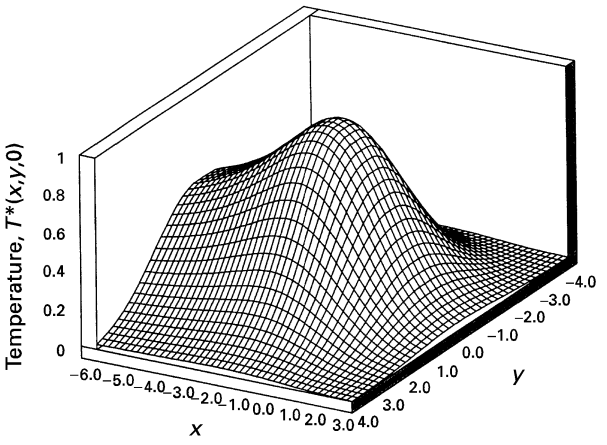

Figure 2 Three-dimensional view of the surface temperature profile for $AP = 600$ W, $U = 53.0$ mm s^{-1}, $r_0 = 3.0$ mm.

TABLE I The material properties of ZrO_2 ceramic used for this study

Properties	ZrO_2	SiO_2	Reference
Density, (kg m^{-3})	5700	2211	[22]
Thermal conductivity, k (W m^{-1} K^{-1})	2.7	1978	[22]
Thermal diffusivity, $\alpha \times 10^{-6}$ (m^2 s^{-1})	0.46	2.51	[22]
Specific heat, c_p (J kg^{-1} K^{-1})	1045		[22]
Melting temperature, T_m (K)	2983	1978	[22]
Absorptivity, A	0.6		
Grain size, r_s (10^{-6} m)	0.5–10		
Surface tension, γ (N m^{-1})	0.4	0.4	[23]
Viscosity, η (N s m^{-2})	10^2–$10^{3.5}$	10^2–$10^{3.5}$	[24]

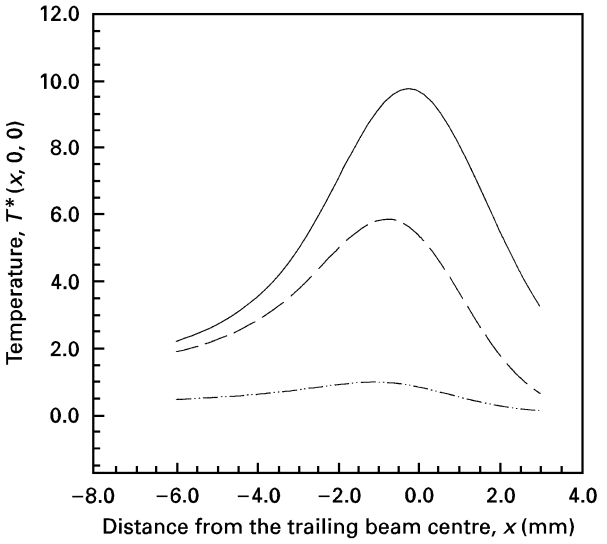

Figure 3 Effects of the laser beam scanning velocity on the surface temperature distribution along the x-axis ($y = 0$, $z = 0$). $AP = 600$ W; $r_0 = 3.0$ mm; (—) $U = 0.1$ mm s^{-1}; (— —) $U = 1.0$ mm s^{-1}; (— · · —) $U = 53.0$ mm s^{-1}.

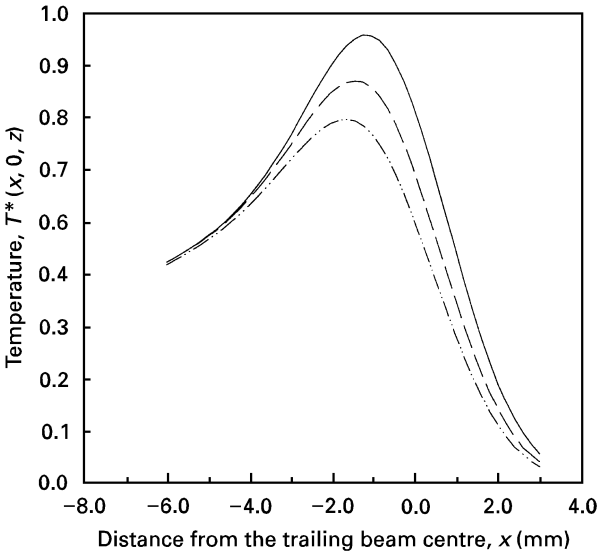

Figure 4 Temperature distribution along the x-axis ($y = 0$) at various depths of the substrate. $AP = 600$ W; $r_0 = 3.0$ mm; $U = 53.0$ mm s^{-1}; (—) $z = 0$ μm; (— —) $z = 15$ μm; (— · · —) $z = 45$ μm.

structure because a Gaussian laser beam is used as the heat source in this study. The peak temperature at the trail of the laser beam reaches 2847 K for absorbed power, $AP = 600$ W, scanning velocity, $U = 53.0$ mm s^{-1}, and laser beam spot radius, $r_0 = 3.0$ mm. This peak temperature is lower than the melting temperature (2983 K) of ZrO_2. Hence, a thin layer of glasslike ZrO_2 is formed near the surface. Moreover, due to the motion of the laser beam in the positive x direction relative to the substrate, advection heat flow occurs in the negative x direction which causes the peak temperature at the substrate to be near the trailing edge rather than at the beam centre.

Fig. 3 indicates the surface temperature distribution along the x-axis for various values of the laser beam scanning velocity. As the velocity increases, the laser-material interaction time decreases which means that less time is available to heat the material, and therefore, the peak temperature decreases. Also, the temperature profile becomes quite asymmetric with respect to the origin, $x = 0$. As the velocity decreases, the effect of advection heat flow decreases and the conduction heat flow becomes dominant, and thus the temperature profile tends to be more symmetric with respect to the origin, and the peak temperature appears at a value of x close to zero. Fig. 3 shows that the surface temperature along the x-axis has a similar distribution for different laser beam scanning velocities, where the peak temperature is located behind the laser beam centre. The higher the laser beam scanning velocity, the further away is the peak temperature from the laser beam centre. The depth of thermal penetration increases as the scanning velocity decreases. For instance, with absorbed power, $AP = 600$ W, $r_0 = 3.0$ mm, $U = 70.0$ mm s^{-1}, only a depth of 5 μm can be heated to the range of 0.75 T_m (at $z = 5$ μm), while for $U = 53.0$ mm s^{-1}, the same temperature range of 0.95 T_m (at $z = 0$ μm) can be attained at a depth of 50 μm.

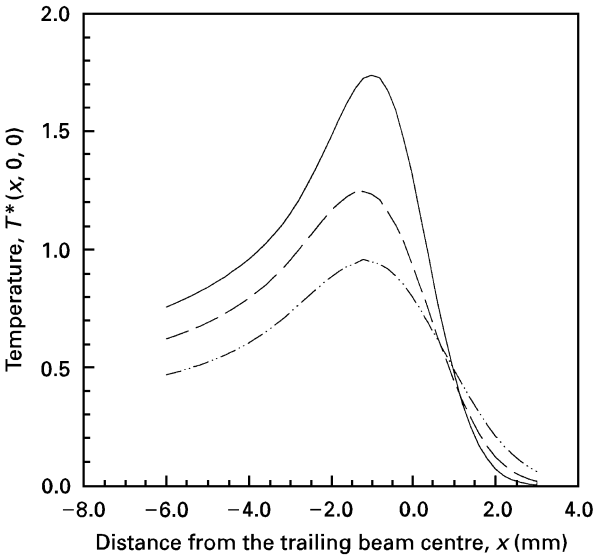

Figure 5 Effects of the laser beam radius on the surface temperature distribution along the x-axis ($y = 0$, $z = 0$). $AP = 600$ W; $U = 53.0$ mm s^{-1}; (—) $r_0 = 2.0$ mm; (— —) $r_0 = 2.5$ mm; (— · · —) $r_0 = 3.0$ mm.

Fig. 4 shows the temperature variations along the x axis for various axial (z) locations. The temperature is very high on the surface and it decreases as z increases. For absorbed power, $AP = 600$ W, $U = 53.0$ mm s^{-1} and $r_0 = 3.0$ mm, the heat-affected zone is found to be about 50 μm in which the ceramic substrate vitrifies. It can be seen in Fig. 4 that the position of the peak temperature at different z locations moves gradually farther away from the trailing beam centre as z increases. Fig. 4 can be used to determine the geometrical shape of the densified zone. It can also be used to determine the microstructure of the vitrified ceramics if the effective phase transformation temperature is known.

Fig. 5 represents the temperature for three different laser beam spot radii, $r_0 = 2.0$, $r_0 = 2.5$, and $r_0 = 3.0$ mm. The larger the beam radius r_0, the lower is the

laser power density. This reduces the peak temperature as the beam radius increases. For the same absorbed power, $AP = 600$ W, and laser beam scanning velocity, $U = 53.0\ \text{mm s}^{-1}$, the magnitude of the temperature gradient around the peak temperature increases as the beam radius decreases because the intensity of the laser beam increases with the decrease in beam radius.

3.2. Temperature distribution using an approximate and simplified expression

Equation 18 is an approximate and simplified expression for the three-dimensional temperature distribution in the workpiece under quasi-steady state condition due to laser heating by a scanning beam. However, the expression has two unknown parameters, k_0 and k_1 that are determined in this study by comparing the approximate solution to the exact solution obtained from Equation 17. Figs 6, 7 and 8 present the coefficients k_0 and k_1 for temperature distribution along the z-axis ($y = 0$) for various values of laser power and beam radii as indicated in these figures. The k_0 and k_1 values were used to calculate temperature when the substrate does not melt. It can be seen that k_0 and k_1 increases as the laser beam scanning velocity U increases (except k_0 at $z = 0$) and it has different values than for different values of z. In Fig. 6, k_0 and k_1 values for $z = 0$ and $U = 53.0\ \text{mm s}^{-1}$ correspond to the peak temperature $0.95\ T_m$. Similarly in Fig. 7, k_0 and k_1 values for $z = 0$ and $U = 78.0\ \text{mm s}^{-1}$ correspond to the peak temperature $0.95\ T_m$. Also, in Fig. 8, k_0 and k_1 values for $z = 0$ and $U = 95.0\ \text{mm s}^{-1}$ correspond to the peak temperature $0.95\ T_m$.

The surface temperature distributions along the x-axis are calculated by using the exact and simplified expressions, and are reported in Figs 9, 10 and 11.

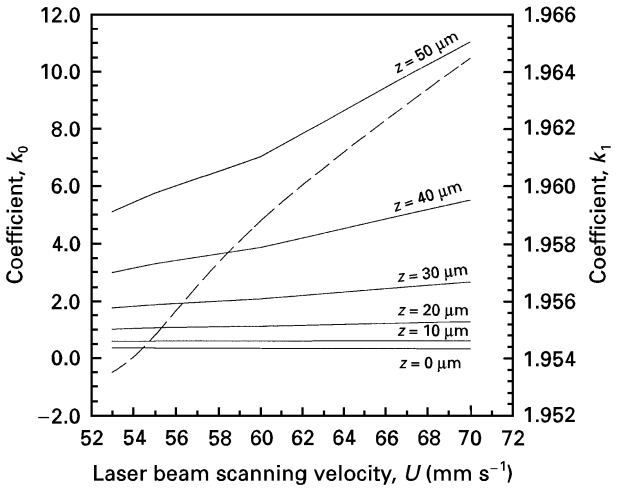

Figure 6 Coefficients k_0 (—), k_1 (— —) for the simplified expression for temperature distribution along the z-axis ($y = 0$). $AP = 600$ W; $r_0 = 3.0$ mm.

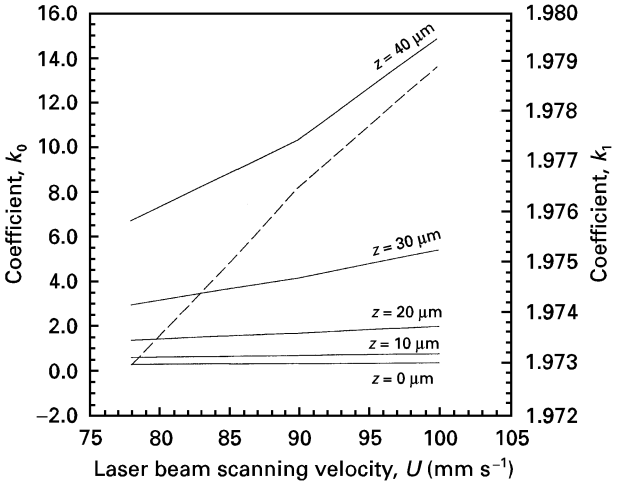

Figure 7 Coefficients k_0 (—), k_1 (— —) for the simplified expression for temperature distribution along the z-axis ($y = 0$). $AP = 900$ W; $r_0 = 3.5$ mm.

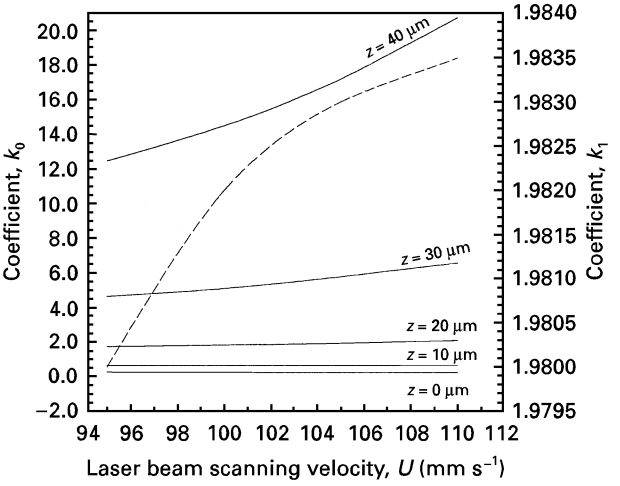

Figure 8 Coefficients k_0 (—), k_1 (— —) for the simplified expression for temperature distribution along the z-axis ($y = 0$). $AP = 1200$ W; $r_0 = 4.0$ mm.

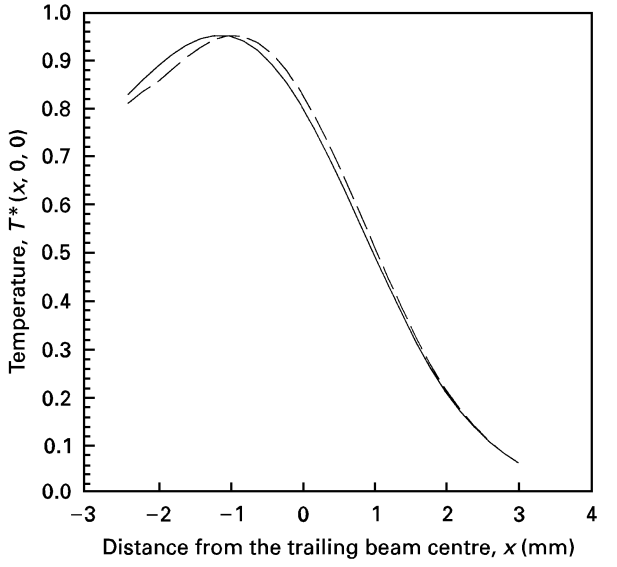

Figure 9 Surface temperature distribution along the x-axis ($y = 0$) calculated from the exact (—) and simplified (— —) solutions. $AP = 600$ W; $r_0 = 3.0$ mm; $U = 53.0\ \text{mm s}^{-1}$.

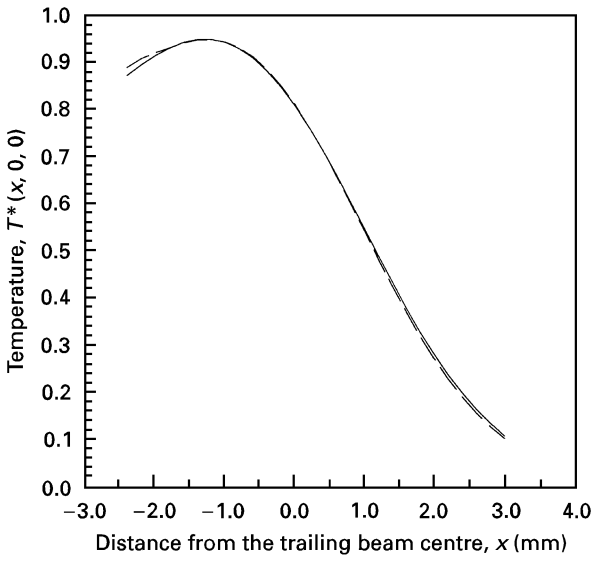

Figure 10 Surface temperature distribution along the x-axis ($y = 0$) calculated from the exact (—) and simplified (——) solutions. $AP = 900$ W; $r_0 = 3.0$ mm; $U = 78$ mm s^{-1}.

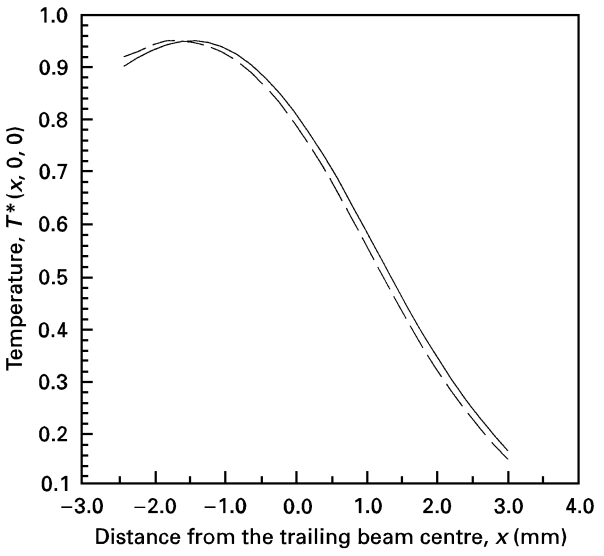

Figure 11 Surface temperature distribution along the x-axis ($y = 0$) calculated from the exact (—) and simplified (——) solutions. $AP = 1200$ W; $r_0 = 4.0$ mm; $U = 95.0$ mm s^{-1}.

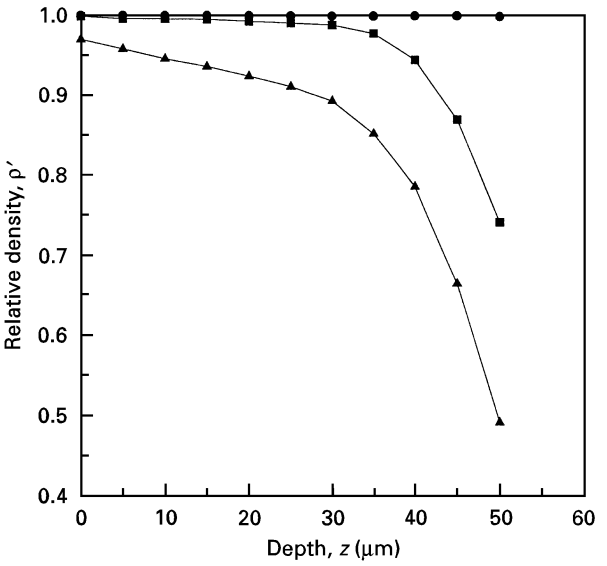

Figure 12 The relative density of the vitrified zone for different initial radii of the ZrO_2 particles in the workpiece (powder compact). $AP = 600$ W; $r_0 = 3.0$ mm; $U = 53.0$ mm s^{-1}; (●) $r_s = 0.5$ μm; (■) $r_s = 5$ μm; (▲) $r_s = 10$ μm.

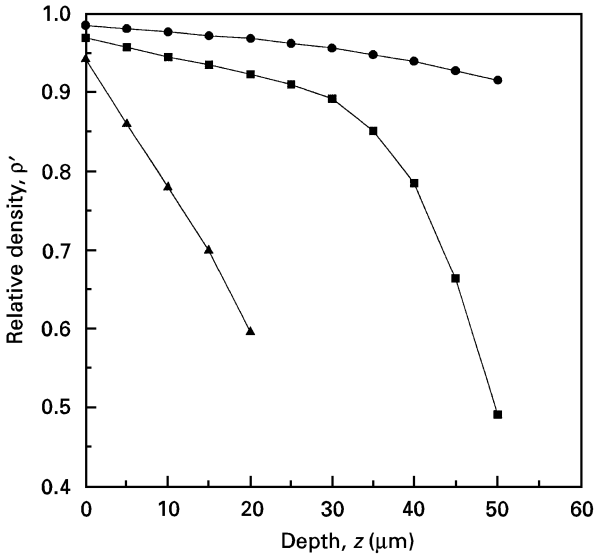

Figure 13 The relative density of the vitrified zone for different absorbed power. $r_0 = 3.0$ mm; $r_s = 10$ μm; $U = 53.0$ mm s^{-1}; (●) $AP = 660$ W; (■) $AP = 600$ W; (▲) $AP = 540$ W.

These figures show that the simplified expression produces fairly accurate temperature distribution for different laser beam parameters and processing conditions in the region defined by $-2.0\text{ mm} \leqslant x \leqslant \infty$, $0 \leqslant z \leqslant 50$ μm and $y = 0$. The difference between the results obtained from the exact and the simplified solutions is found to be within 10%.

3.3. Effects of process parameters on densification

Equation 20 is used to calculate the relative density distribution in the ZrO_2 ceramic substrate by using the data listed in Table I. Due to the lack of data for surface tension (γ) and viscosity (η) of ZrO_2 at high temperatures, the data for SiO_2 at a high temperature ($0.85T_m$) is used in this study since the thermophysical properties, such as k and α, of SiO_2 and ZrO_2 are similar.

Figs 12, 13, 14 and 15 represent the relative density profile in the vitrified region for various processing conditions. It can be seen that relative density is maximum at the top surface of the substrate, and it decreases as the depth increases. The corresponding 10–40 μm thick vitrified layer is densified to reach a relative density of about 0.95. The surface of the substrate is almost fully densified for all three different particle sizes. Additionally, it can be seen in Fig. 12 that the relative density of the vitrified zone increases with decreasing particle size. When the nominal particle size is changed from 10 μm to 1 μm, the depth having the same relative density increases from 10 μm to 40 μm.

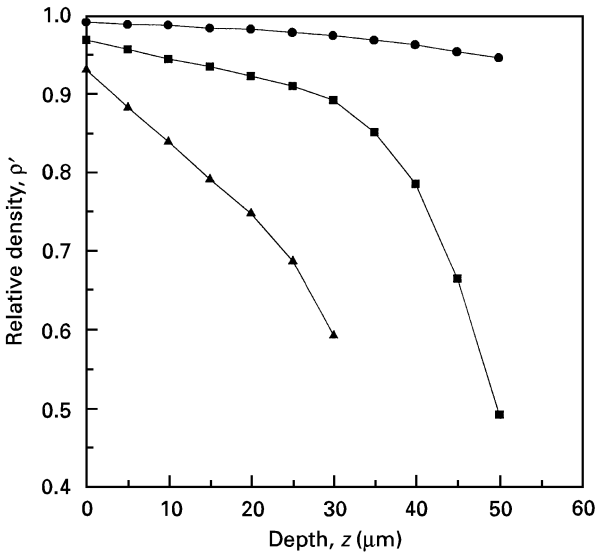

Figure 14 The relative density of the vitrified zone for different laser beam scanning velocities. $AP = 600$ W; $r_0 = 3.0$ mm; $r_s = 10$ μm; (●) $U = 45.0\ \text{mm s}^{-1}$; (■) $U = 53.0\ \text{mm s}^{-1}$; (▲) $U = 60.0\ \text{mm s}^{-1}$.

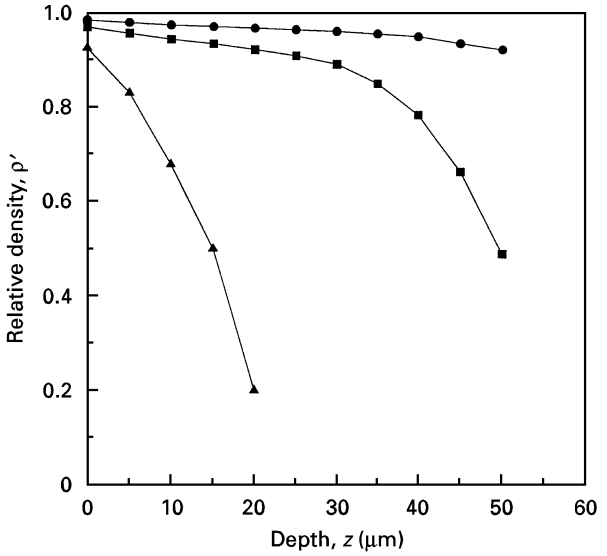

Figure 15 The relative density of the vitrified zone for different laser beam spot radii. $AP = 600$ W; $r_s = 10$ μm; $U = 53.0\ \text{mm s}^{-1}$; (●) $r_0 = 2.75$ mm; (■) $r_0 = 3.0$ mm; (▲) $r_0 = 3.25$ mm.

3.4. Experimental verification

Petitbon and Boquet [21] conducted a surface densification experiment by melting a thin layer of zirconia coating with a continuous wave CO_2 laser beam. They reported that laser-induced rapid surface melting and solidification can generate a 30–50 μm fully dense layer of 13 GPa hardness with fine and homogeneous microstructures, but that it can also generate serious cracking problems due to shrinkage and differential stresses. It was proposed that chemical modifications of the treated surface might eliminate the cracking problem. They obtained best results by injecting alumina powder into the laser–substrate interaction zone. By adjusting the beam parameters and powder flow rate, an alumina–zirconia eutectic can be formed at the surface leading to a greatly strengthened surface composite. For low powers and long interaction times, they found that the treated surface was smooth, dense and very hard (20 GPa) with reduced microcracks. They induced densification to a depth of 30 μm ~ 50 μm in ZrO_2 substrate for laser power, $P = 3$ kW, beam radius, $r_0 = 1.5 \sim 2.5$ mm and scanning velocity, $U = 40.0 \sim 66.0\ \text{mm s}^{-1}$. The theoretical results for the thickness of the vitrified layer predicted by the model of this paper with laser power, $P = 3$ kW, beam radius, $r_0 = 2.0$ mm and scanning velocity, $U = 53.0\ \text{mm s}^{-1}$ is found to be 50 μm for the absorptivity $A = 11\%$. This shows that the prediction of this model agrees well with experimental data.

4. Conclusions

A three-dimensional quasi-steady state heat conduction model is presented for calculating the temperature distribution and the relative density of ZrO_2 ceramic coating due to the TEM_{00} mode laser-induced densification. The heat conduction problem is solved by using the Fourier transform to obtain an integral expression for the temperature field. The integrals of this expression are evaluated numerically by using the trapezoidal rule for numerical integration. The effects of different process parameters on the calculated temperature distribution in the substrate are investigated. By carefully selecting the laser power, beam radius and scanning velocity, the maximum temperature at the substrate surface can be made to reach $0.95T_m$ in order to achieve densification through the vitrification process – densification with the aid of a viscous liquid phase. This results in a dense top layer at the substrate surface. The depth of densification is strongly affected by the initial radius of the particle in the workpiece (powder compact) for a given temperature distribution.

Appendix: Derivation of approximate expression (Equation 18) from exact temperature distribution (Equation 17)

$$\frac{\exp[-b(r'^2+z^2)^{1/2}]}{(r'^2+z^2)^{1/2}}\,r'$$

$$= \frac{r'}{(r'^2+z^2)^{1/2}} \exp\{-b[(r'+z)^2 - 2r'z]^{1/2}\}$$

$$\approx k_0 \exp[-b(r'+z)]$$

for small values of z. Equation 17 can now be written as

$$T^*(x,y,z) = \frac{2PA}{(\pi r_0)^2 k(T_m - T_0)} k_0 \exp(-bz) \times \int_0^{\pi}\int_0^{\infty} \exp(-br') \exp\left\{-\frac{2r'^2}{r_0^2} - \left[b\cos\phi - \frac{4(x\cos\phi + y\sin\phi)}{r_0^2}\right]r' - \frac{2x^2+2y^2}{r_0^2}\right\} dr'\,d\phi$$

$$= \frac{2PA}{(\pi r_0)^2 k(T_m - T_0)} k_0 \exp(-bz) \times \exp\left(-\frac{2x^2 + 2y^2}{r_0^2}\right) \int_0^{\pi} \int_0^{\infty} \exp\left\{-\frac{2r'^2}{r_0^2} - \left[b + b\cos\phi - \frac{4(x\cos\phi + y\sin\phi)}{r_0^2}\right] r'\right\} dr'\, d\phi \quad \text{(A1)}$$

Define

$$F = \int_0^{\pi} \int_0^{\infty} \exp\left\{-\frac{2r'^2}{r_0^2} - \left[b + b\cos\phi - \frac{4(x\cos\phi + y\sin\phi)}{r_0^2}\right] r'\right\} dr'\, d\phi$$

In the regions $0 \leqslant \phi \leqslant \pi/2$ and $\pi/2 \leqslant \phi \leqslant \pi$, the mean value of $\sin\phi$ is $1/2$; and the mean value of $\cos\phi$ are $1/2\,k_1$ and $-1/2\,k_1$, respectively. F is now approximated as

$$F \approx \int_0^{\infty} \exp\left(-\frac{2r'^2}{r_0^2}\right) \exp(-br')\, dr' \times \left\{\int_0^{\pi/2} \exp\left(-br'\frac{1}{2}k_1\right) \exp\left[\frac{4(x\frac{1}{2}k_1 + \frac{1}{2}y)}{r_0^2}\right] + \int_{\pi/2}^{\pi} \exp\left(br'\frac{1}{2}k_1\right) \exp\left[\frac{4(-x\frac{1}{2}k_1 + \frac{1}{2}y)}{r_0^2}\right] d\phi\right\}$$

$$= \frac{\pi}{2}\left\{\int_0^{\infty} \exp\left[-\frac{2r'^2}{r_0^2} - \left(b + \frac{1}{2}bk_1 - \frac{2(xk_1 + y)}{r_0^2}\right) r'\right] + \int_0^{\infty} \exp\left[-\frac{2r'^2}{r_0^2} - \left(b - \frac{1}{2}bk_1 + \frac{2(xk_1 - y)}{r_0^2}\right) r'\right]\right\} \quad \text{(A2)}$$

By using the integral formula

$$\int_0^{\infty} \exp(-ax^2 - bx)\, dx = \frac{1}{2}\left(\frac{\pi}{a}\right)^{1/2} \exp\left(-\frac{b^2}{4a}\right) \operatorname{erfc}\left(\frac{b}{2a^{1/2}}\right)$$

in Equation A2, F can be written as

$$F = \frac{\pi}{4}\left(\frac{r_0^2\pi}{2}\right)^{1/2} \left\{\exp\left(\left[b + \frac{1}{2}bk_1 - \frac{2(xk_1 + y)}{r_0^2}\right]^2 \Big/ (8/r_0^2)\right) \operatorname{erfc}\left(\left[b + \frac{1}{2}bk_1 - \frac{2(xk_1 + y)}{r_0^2}\right] \Big/ \left(\frac{8}{r_0^2}\right)^{1/2}\right) + \exp\left(\left[b - \frac{1}{2}bk_1 + \frac{2(xk_1 - y)}{r_0^2}\right]^2 \Big/ (8/r_0^2)\right) \times \operatorname{erfc}\left[b - \frac{1}{2}bk_1 + \frac{2(xk_1 - y)}{r_0^2} \Big/ \left(\frac{8}{r_0^2}\right)^{1/2}\right]\right\} \quad \text{(A3)}$$

Noting that $\operatorname{erfc}(x) = e^{-x^2}/(\pi x)^{1/2}[1 + \sum_{n=1}^{\infty}(-1)^n (1\cdot 3\cdot\cdots\cdot(2n-1)/(2x^2)^n)]$ and using only the first term of this series expansion, Equation A3 is simplified as

$$F = \frac{\pi}{2}\left\{1 \Big/ \left[b + \frac{1}{2}bk_1 - \frac{2(xk_1 + y)}{r_0^2}\right] + 1 \Big/ \left[b - \frac{1}{2}bk_1 + \frac{2(xk_1 - y)}{r_0^2}\right]\right\} \quad \text{(A4)}$$

Substituting Equation A4 into Equation A1, the approximate and simplified expression for the temperature distribution is given by

$$T^*(x, y, z) = \frac{PA}{\pi r_0^2 k(T_m - T_i)} \times k_0 \exp(-bz) \exp\left(-\frac{2x^2 + 2y^2}{r_0^2}\right) \times \left\{1 \Big/ \left[b + \frac{1}{2}bk_1 - \frac{2(xk_1 + y)}{r_0^2}\right] + 1 \Big/ \left[b - \frac{1}{2}bk_1 + \frac{2(xk_1 - y)}{r_0^2}\right]\right\}$$

Acknowledgements

The authors gratefully acknowledge the financial support provided by the Mechanical, Materials and Aerospace Engineering Department and the Center for Research and Education in Optics and Lasers at the University of Central Florida.

References

1. H. E. CLINE and T. R. ANTHONY, *J. Appl. Phys.* **48** (1977) 3895.
2. M. LAX, *ibid.* **48** (1977) 3919.
3. *Idem.*, *Appl. Phys. Lett.* **33** (1978) 786.
4. H. S. CARSLAW and J. C. JAEGER, "Conduction of heat in solids", 2nd edition (Clarendon Press, Oxford, 1959) p. 10.
5. L. D. HESS, R. A. FORBER, S. A. KOKOROWSHI and G. L. OLSON, in Proceedings of The Society of Photo-Optical Instrumentation Engineers, edited by J. F. Ready (Society of Photo-Optical Instrumentation Engineers, Washington DC, 1980) p. 31.
6. Y. I. NISSIM, A. LIETOILA, R. B. GOLD and J. F. R. GIBONS, *J. Appl. Phys.* **51** (1980) 274.
7. J. E. MOODY and R. H. HENDEL, *ibid.* **53** (1982) 4364.
8. M. F. MODEST and H. ABAKIANS, *J. Heat Transfer* **108** (1986) 597.
9. C. MAIER, P. SCHAAF and U. GONSER, *Mater. Sci. Engng* **A150** (1992) 271.
10. D. J. SANDERS, *Appl. Optics* **23** (1984) 30.
11. A. KAR and J. MAZUMBER, *J. Appl. Phys.* **65** (1989) 2923.
12. O. MANCA, B. MORRONE and V. NASO, *Int. J. Heat Mass Transfer* **38** (1995) 1305.
13. TAIPAU CHIA, L. L. HENCH, CHAOBIN QIN and C. K. HSIEH, *Mater. Res. Soc. Symp. Proc.* **180** (1990) 819.
14. M. OKUTOMI and K. TSUKAMOTO, *Proc. LAMP* (May 1987) 595.
15. T. KASAI, Y. OZAKI, H. NOD, K. KAWASAKI and K. TANEMOTO, *J. Amer. Ceram. Soc.* **72** (1989) 1716.
16. A. KAR, J. E. SCOTT and W. P. LATHAM, *J. Appl. Phys.* **80** (1996) 667.
17. M. NECATI OZISIK, "Heat conduction" (John Wiley and Sons, New York, 1980) p. 632.
18. J. HECHT, "Understanding laser " (Howard W. Sams & Company, Indianapolis, 1988) p. 83.
19. D. W. RICHERSON, "Modern ceramic engineering" (Marcel Dekker, Inc., New York, 1982) p. 219, p. 531.

20. W. D. KINGERY, H. K. BOWEN and D. R. UHLMANN, "Introduction to ceramics" (John Wiley & Sons, New York, 1976) p. 490.
21. A. PETITBON and D. GUIGNOT, U. FISCHER and J. M. GUILLEMONT, *Mater. Sci. Engng* **A121** (1989) 545.
22. Y. S. TOULOLKIAN (ed.) "Thermophysical properties of the high temperature solid materials. Vol. 4, oxides and their solutions and mixtures, Part I: Simple oxygen compounds and their mixture" (The Macmillan Company, New York, 1967) p. 571.
23. N. P. BANSAL and R. H. DOREMUS, "Handbook of glass properties" (Academic Press, Inc., Orlando, 1986) p. 107.
24. J. D. WALTON, jr. "Radome engineering handbook design and principles" (Marcel Dekker, Inc., New York, 1970) p. 281.

Received 13 May 1996
and accepted 9 May 1997